Acta Materialia 98 (2015) 391–404

Contents lists available at ScienceDirect

Acta Materialia

journal homepage: www.elsevier.com/locate/actamat

Size and orientation effects in partial dislocation-mediated deformation of twinning-induced plasticity steel micro-pillars

Won Seok Choi [a], Bruno C. De Cooman [a,*], Stefanie Sandlöbes [b], Dierk Raabe [b]

[a] Graduate Institute of Ferrous Technology, Pohang University of Science and Technology, Pohang, Republic of Korea
[b] Max-Planck-Institut für Eisenforschung GmbH, Düsseldorf, Germany

ARTICLE INFO

Article history:
Received 22 January 2015
Revised 14 April 2015
Accepted 5 June 2015
Available online 8 August 2015

Keywords:
TWIP steel
Micro-pillar
Micro-compression
Twinning
Twin nucleation

ABSTRACT

Bulk and micro-pillar single crystals were used to investigate the twinning-induced plasticity mechanism in austenitic Fe-22 wt%Mn-0.6 wt%C TWIP steel. Compression of micro-pillars oriented either for deformation-induced twinning or for perfect dislocation glide was carried out for pillars with diameters in the range of 600 nm to 4 μm. The same size dependence of the critical resolved shear stress was observed for both orientations. The critical micro-pillar diameter for size-independent plasticity was approximately 7.6 μm. Partial dislocation-mediated formation of twins and ε-martensite was observed in micro-pillars oriented for twinning by transmission electron microscopy. The elastic–plastic transition in micro-pillars oriented for deformation twinning did not involve twinning, and dislocation–dislocation interactions were a necessary precondition for twin formation.

1. Introduction

The classical theories for deformation twinning in face centered cubic (fcc) metals and alloys assume that twinning is initiated in high stress conditions, in stage III hardening, at low temperatures or in high strain rate deformation conditions [1]. The twin orientation is achieved by a homogeneous shearing of the matrix, which requires the highly coordinated glide of $\frac{a}{6}<1\ 1\ 2>$-type partial dislocations with the same Burgers vector, with exactly one dislocation gliding on each successive {1 1 1}-type twinning planes. Twinning is initiated after slip on the primary slip system and the conjugate system has occurred and a high stress is available to activate the twin nuclei formed by dislocation interactions. The twin formation modifies the prior dislocation structure, with some initially glissile dislocations of the parent crystal being transformed to sessile dislocations in the twin. The Burgers vector of some dislocations may change when they are transformed in the twin matrix. This process contributes to the strain hardening of the deformation twins [2]. In addition, the dynamic Hall–Petch effect [3] also contributes to strain hardening in polycrystals undergoing deformation twinning as twin boundaries are strong obstacles to glide and the formation of micro-twins gradually reduces the dislocation mean free path. Mechanical twinning in fcc metals does not twin single crystals or grains entirely, and the deformed microstructure always contains layers with the parent orientation alternating with twinned ones.

Several deformation twin formation mechanisms have been proposed for polycrystalline metals and alloys, such as the emission of dislocations from periodic grain boundaries ledges, which assumes that twins can be generated directly, without the need to form suitable dislocation junctions [4–7]. Using molecular dynamics and discrete dislocation dynamics simulation, Weinberger et al. [8] argued that the emission of surface dislocations, nucleated at atomically sharp corners, compensates for dislocation starvation during the deformation of micro-pillars in which dislocation starvation occurs. Zhu et al. [9] also argued in favor of twinning by partial dislocation nucleation at surfaces, but they did not propose an actual mechanism for the generation of partial dislocations from surfaces. There are fundamental problems with the assumption that surfaces or grain boundaries can be a source of twinning dislocations, such as the fact that the emission of a partial dislocation loop requires a high critical shear stress, and that twin formation requires a precise partial dislocation sequence, i.e. one single partial dislocation on every {1 1 1} type slip plane. Partial dislocation emission from a surface has not conclusively been shown to be compatible with these requirements.

When small scale compression testing (in a nano-indentation setup) is used to analyze the deformation of micro-pillars, a characteristic size effect is observed [10,11]: the shear stress to initiate plastic flow increases with decreasing pillar diameter [12–17]. Greer et al. [12] proposed a dislocation starvation model to explain

* Corresponding author.
E-mail address: decooman@postech.ac.kr (B.C. De Cooman).

http://dx.doi.org/10.1016/j.actamat.2015.06.065
1359-6454/

the size effect. Dislocation source-hardening, which occurs in small samples due to the physical limitation of the dislocation source size, was proposed to account for the considerable strengthening in micron-sized single crystals [13]. The size dependence of the strength of single-ended dislocation sources was verified by three-dimensional discrete dislocation dynamics simulation [14]. Yu et al. [15] reported that the twinning stress in micro-pillars was also size-dependent. Seo et al. [16] reported that the strength of Au nano-wires, in which twins were formed, was inversely related to their diameter. Size effects were also reported for TWIP steel micro-pillars deformed in compression [17].

In the present study, the twinning-induced plasticity mechanism of TWIP steel was studied by means of compression tests on bulk single crystals and micro-pillars, oriented either for perfect dislocation glide or, respectively, for deformation twinning. Transmission electron microscopy (TEM) was used to investigate dislocation interactions and the evolution of the deformation microstructure in the micro-pillars. The dislocation interactions were characterized at the initial stage of the deformation in which no microstructural evolution had occurred in order to verify whether the yielding mechanism of the micro-pillars was associated with twin formation.

2. Experimental procedure

Bulk single crystals of a Fe-22 wt%Mn-0.6 wt%C TWIP steel [18,19], with a stacking fault energy (SFE) of 23 mJ/m^2 [20] were grown by the Bridgman technique with a [011] and a [001] orientation. Perfect dislocation glide is preferred in [110]-oriented crystals when subjected to compression deformation. Mechanical twinning is preferred during compression deformation in [001]-oriented crystals.

Micro-pillars oriented either for perfect dislocation glide or for deformation twinning in compressive deformation were also produced. The micropillars with a height-to-diameter aspect ratio of 2–3 [11], were fabricated by the focused ion beam (FIB) technique. A 10 pA milling current was used for final milling to obtain a taper angle smaller than 4° and minimize the surface damage caused by the Ga$^+$ ion beam. The top diameter of the micro-pillars, which was used to calculate the reported stresses, varied from 0.6 to 4.0 μm.

The micro-pillars were produced from areas of the single crystals for which the orientation was determined by electron back-scatter diffraction (EBSD) in a FEI Quanta 3D FEG SEM. The stereographic triangle shown in Fig. 1a presents the orientation information of the micro-pillars. The stress on the leading and trailing partial dislocations depends on the orientation of the compression axis and the difference in the stress will affect the stacking fault width [21,22]. The Schmid factors for the perfect and partial dislocations associated with the primary slip system are listed in Table 1 for the bulk single crystals and the micro-pillars taking compression deformation into account. The Schmid factor of the leading and trailing partial dislocations of the primary slip system for the [5422]-oriented micro-pillar was 0.49 and 0.26, respectively, indicating that the effective stacking fault width between the partials ***Aδ*** and ***δC*** was larger than the stress-free partial dislocation separation during compression (Fig. 1b). In the case of the [16623]-oriented micro-pillar, the screw-oriented perfect dislocation ***DB*** segments were expected to glide with a reduced dissociation width (Fig. 1c) because the force on the trailing partial was larger than on the leading partial.

The compression tests on the bulk single crystals were conducted on a Zwick/Roell universal testing machine using a strain rate of 10^{-3} s^{-1}. The compression tests on the micro-pillars were carried out on a PI 85 SEM Pico-Indenter. The indenter tool used to impose the compressive state was operated in load control mode, i.e. at constant loading rate. The strain rate was 10^{-3} s^{-1} in the initial deformation stages. A flat diamond punch tip with a diameter of 10 μm was used as tool. The Berkovich micro-indentation technique was utilized to determine the shear modulus for the [16623] and [5422] oriented grains in the areas where the micro-pillars were made. The reported values are average values of 10 measurements. The standard deviation was 10.1 GPa and 8.3 GPa for the [16623] and [5422] grains, respectively.

The morphology of the deformed micro-pillars was analyzed in a ZEISS field emission Ultra-55 SEM before and after the compression tests. Saw cuts parallel to the most prominent slip trace were obtained from compressed bulk single crystal to make TEM samples in which the electron beam was parallel to the <111> direction. TEM samples were taken from the micro-pillars parallel to

Table 1
Orientation dependence of the Schmid factor for bulk single crystals and micro-pillars of TWIP steel.

Compression axis	Schmid factor		
	Perfect	Leading partial	Trailing partial
Micro-pillar [5422]	0.43, AC	0.49, δC	0.26, Aδ
Micro-pillar [16623]	0.47, DB	0.34, αB	0.48, Dα
Single crystal [001]	0.41	0.47	0.24
Single crystal [011]	0.41	0.24	0.47

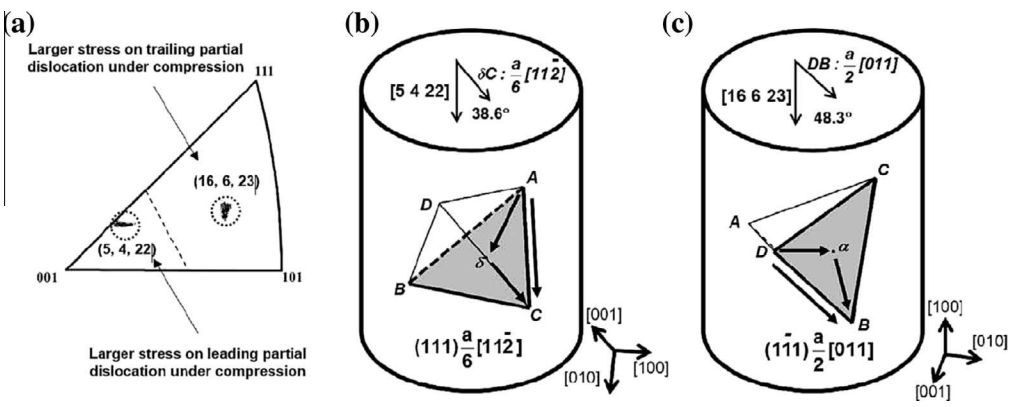

Fig. 1. Crystallographic orientation of the micropillars tested under compression by using a nano-indentation setup and corresponding Thompson tetrahedra. (a) Crystallographic orientation of the micropillars. (b) Primary slip system in the [5422]-oriented micropillar. ABC (111) is the primary slip plane and the leading twinning partial dislocation is δC $\frac{a}{6}[11\bar{2}]$. (c) Primary slip system in the [16623]-oriented micropillar. BCD ($\bar{1}$1$\bar{1}$) is the primary slip plane and glide is by the motion of perfect dislocation with a Burgers vector DB $\frac{a}{2}$[011].

the [1 1 0] and [$\bar{1}$ 1 0] directions by means of FIB sample preparation. A 400 V Ar^+ ion cleaning step using the Technoorg Linda Gentle Mill was used to remove the surface damage due to the FIB sample fabrication. The TEM observations were carried out in a JEOL JEM-2100F operated at 200 kV and a Philips CM20 operated at 200 kV.

3. Results

3.1. Bulk single crystal and micro-pillar compression

Fig. 2a and b show the uniaxial compression test results for a representative bulk single crystal and micro-pillars with a diameter in the range of 0.6–4.0 μm. It is clear that the yield stress of the micro-pillars was considerably higher than the yield stress of the single crystal and that the yield stress increased with decreasing pillar diameter. Inspection of the load curves revealed multiple strain bursts. The strain bursts were separated by regions of elastic or near-elastic loading. Yielding was initiated by small amounts of plastic activity indicated by a first small strain burst. Multiple strain bursts of various size occurred after yielding. The strain bursts are most likely associated with the formation of mobile dislocation avalanches by dislocation sources [23]. The limited amount of strain observed at the strain bursts suggests that dislocation exhaustion or backstresses suppress further plastic deformation. The very large strain bursts at high stresses cause local shearing of the pillars. The first small strain plateaus present in the initial stage of deformation were considered to correspond to the yield point of the micro-pillars and the corresponding stress was used to determine the critical resolved shear stress reported in the present work. These initial strain plateaus are indicated in Fig. 2c and d. The first micro-strain burst occurred typically at an engineering strain in the range of 0.5–1.5%. The average size of the first strain plateau was about 0.02%. No strain bursts were observed in the case of bulk single crystals. The yield stresses were 187 MPa and 153 MPa for [0 1 1] and [0 0 1] oriented bulk single crystals, respectively. This corresponds to a bulk critical resolved shear stress of 76 MPa and 72 MPa, respectively.

Fig. 3 shows the accumulated plastic strain associated with the strain bursts as a function of the shear stress at which the individual strain bursts occurred for individual micro-pillars. Each line corresponds to a micro-pillar with a specific diameter, oriented either for perfect dislocation glide or deformation twinning. The double logarithmic scale was used to better identify possible differences between the different micro-pillar orientations. The spread in the size of the strain bursts and the strain burst stress clearly increased with decreasing micro-pillar size. This general trend of the stress dependence of the accumulated plastic strain bursts was, however, independent of the micro-pillar orientation. Fig. 4 shows the average value of the first burst stress versus the average value of the first burst strain as a function of micro-pillar size and orientation. As stated earlier, the average value of the first burst stress was considered to be the critical resolved shear stress of the micro-pillar. The critical shear stress of micro-pillars oriented for deformation twinning and perfect dislocation glide were clearly very similar, if not identical, within experimentally acceptable variations. The data given in Fig. 4 shows also clearly that the variations in the value of the critical resolved shear stress and the corresponding strain burst increased considerably with decreasing micro-pillar size.

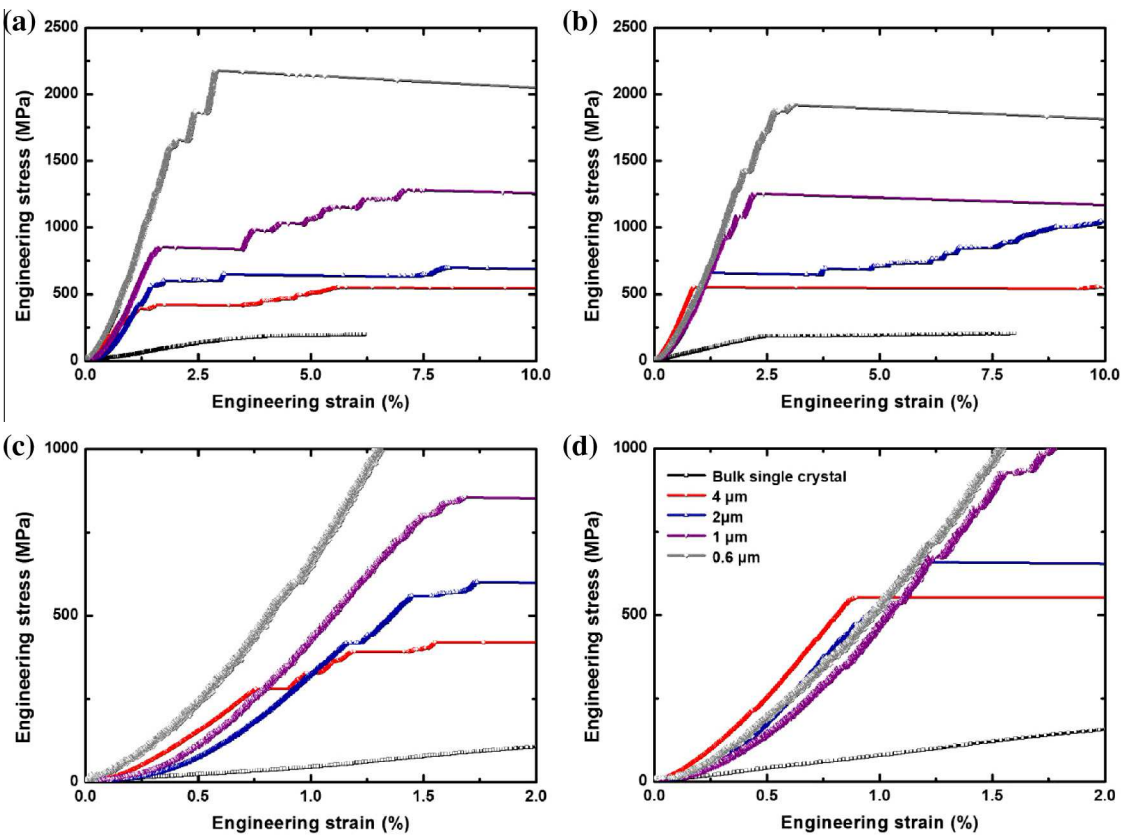

Fig. 2. (a) Uniaxial compression test results for [5 4 22] micropillars oriented for mechanical twinning. (b) Uniaxial compression test results for [16 6 23] micropillars oriented for dislocation glide. (c) Enlargement of the stress–strain curves in (a) in the strain range of 0–2% engineering strain. (d) Enlargement of the stress–strain curves in (b) in the strain range of 0–2% engineering strain. The enlargements in (c) and (d) reveal multiple small strain bursts at low stress levels. The graphs include a representative stress–strain curve for a bulk single crystal (open square symbols).

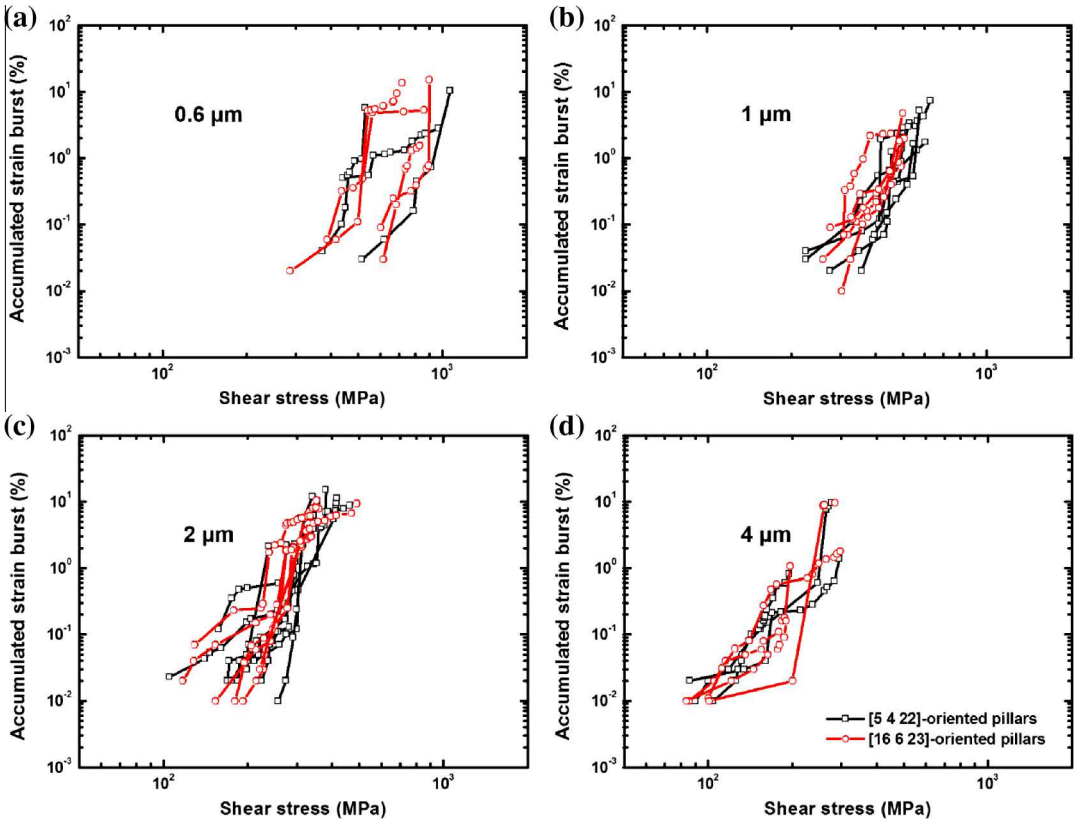

Fig. 3. Accumulated plastic strain burst and corresponding shear stresses of micropillars with a diameter of (a) 0.6 μm, (b) 1 μm, (c) 2 μm, and (d) 4 μm. The spread in the size of the strain burst and the corresponding value of the stress becomes wider as the size of the micropillars decreases. The trend is independent of the orientation of the micropillars.

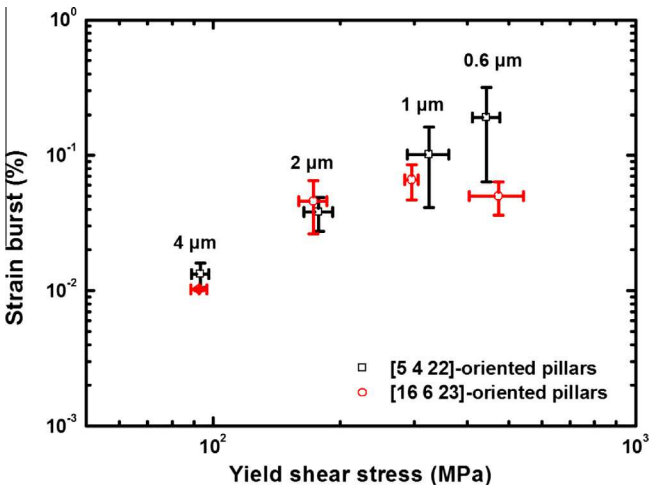

Fig. 4. Average yielding shear stress and corresponding average strain burst of micropillars of different diameters and orientation. The critical resolved shear stress for micro-yielding is similar for the [5422] micropillars, oriented for deformation twinning, and the [16623] micropillars, oriented for dislocation glide. The spread in the value of the critical shear stress and the critical strain burst increases with decreasing micropillar size.

The measurement of the yield strength of micro-pillars is subject to an increasing variability with decreasing pillar diameter. Assuming a dislocation density ρ_d in the range of 10^{11}–10^{10}m^{-2}, the corresponding dislocation spacing, i.e. $\rho_d^{-1/2}$, is in the range of 3–10 μm. Micropillars with a diameter in this size range are expected to exhibit a pronounced size dependence of the yield stress when the pillar diameter is reduced. The variability in the individual measurements of the yield stress should also increase, as the individual pillars will progressively contain fewer and smaller dislocation sources. This general evolution in yield strength will however also have an increased randomness related to the position where the micro-pillars are machined out of a larger crystal. Stress–strain curves, similar to the one shown in Fig. 3 consisting of separated horizontal strain bursts separated by elastic stress–strain segments, have been observed previously by Rinaldi et al. for nano-crystalline Ni nm-size pillars [24] and Mompiou et al. for sub-micron Al-fibers [25]. These authors consider that micro-pillar yielding takes place during the first observable strain burst due to the activation of a single source. The absence of strain hardening in the horizontal strain bursts, suggests that the dislocations emitted by the active source are rapidly eliminated at the pillar surface. At smaller pillar size the yielding should become more sensitive to the statistical distribution of source lengths: (a) the yield stress should increase as larger sources will be less likely in smaller sized pillars, and (b) there should be more variability in the measured yield stress, as the largest source size present in the pillar is randomly selected during pillar manufacturing. This clearly indicates that the initial dislocation source density and the size distribution of the dislocation sources, in particular the size of the largest source present in the pillar, will affect the yield stress measurements.

3.2. Micro-pillar shape

The shapes of a compressed bulk single crystal and of a set of micro-pillars with different diameters are shown in Fig. 5. Fig. 5a shows a [011]-oriented bulk single crystal with a diameter of 4 mm deformed 4% in compression. Clear slip traces were visible

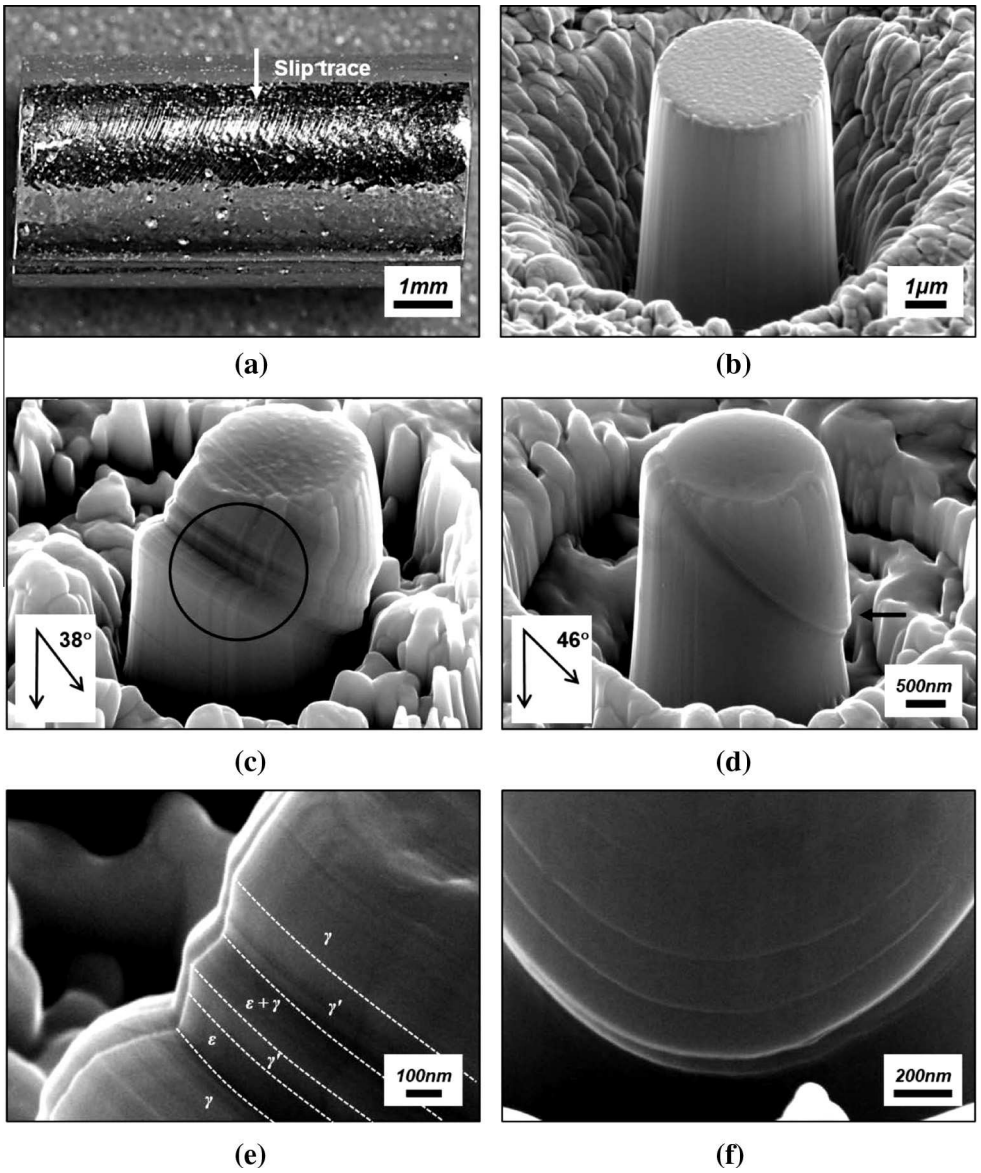

Fig. 5. SEM micrograph of (a) a bulk single crystal deformed 4% in compression along the [0 1 1] direction. (b) Undeformed micropillar with a diameter of 4 μm. (c) Deformed micropillar with 2 μm diameter, [5 4 2 2] oriented for deformation twinning in compression. (d) 2 μm [16 6 2 3] micropillar, oriented for perfect dislocation glide in compression. Enlarged images of the main deformation zones in (c) and (d) are shown in (e) and (f), respectively. The deformation zone in the [5 4 2 2]-oriented micropillars was very wide. The deformation zone in the [16 6 2 3]-oriented micropillar was highly localized. The location of the ε-martensite plates and the mechanical twins formed during compression deformation of the [5 4 2 2]-oriented micropillar is indicated in (e).

on the deformed crystal surface. An undeformed micro-pillar with a diameter of 4 μm is shown in Fig. 5b. In the case of the 2 μm micro-pillars oriented for deformation twinning, the deformation zone was very wide (Fig. 5c), with wide shear-type steps. The deformation of the 2 μm diameter micro-pillar oriented for perfect dislocation glide was highly localized in a narrow shear band (Fig. 5d). The side view of this micro-pillar (Fig. 5f) showed wavy slip traces. These wavy slip traces are indicative of cross-slip of screw dislocations during plastic deformation. The occurrence of wavy slip traces in a medium SFE fcc alloy, such as the Fe-22%Mn-0.6%C TWIP steel used in the present work, points to a reduction of the stacking fault width which facilitates cross slip. The angle between the compression axis and the normal of the primary slip plane or twinning plane was in good agreement with the calculated values of 38° and 46° for the crystals oriented for deformation twinning and perfect dislocation glide, respectively.

3.3. TEM microanalysis

Fig. 6 shows TEM micrographs of plastically deformed bulk single crystals oriented for perfect dislocation glide, and deformation twinning in a compression test involving less than 4% strain. In the sample of the crystal oriented for perfect dislocation glide, the secondary slip system was also activated and the dislocations on the primary and secondary slip plane interacted with each other. Wide stacking faults resulting from partial dislocation glide were observed in the bulk single crystal oriented for mechanical twinning. Even though perfect dislocation glide and partial dislocation-mediated deformation resulting from dislocation break-away were observed as expected in accordance to the crystal orientation, the critical shear stress was very similar in both cases. This suggests that yielding was controlled by the same mechanism in both cases (Fig. 2).

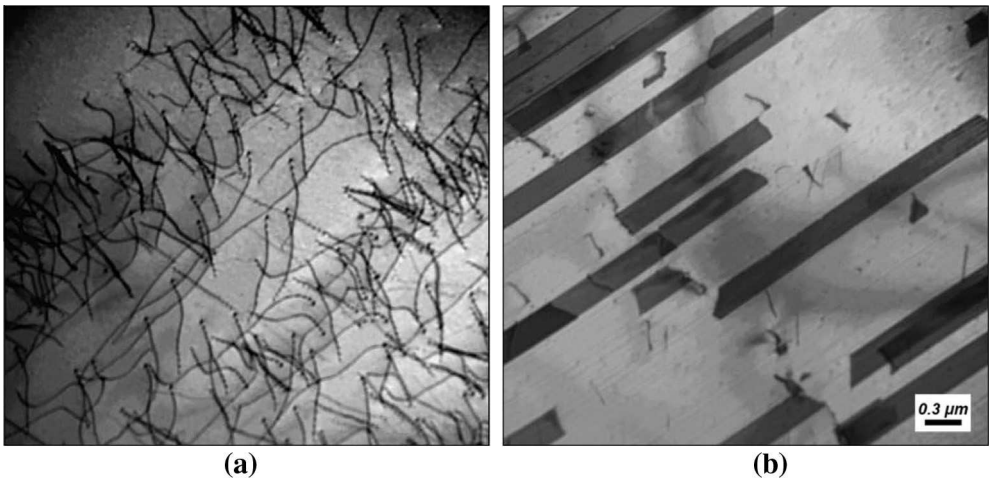

Fig. 6. TEM micrographs of deformed bulk single crystal. (a) Bulk single crystal oriented for dislocation glide showing plastic deformation by perfect dislocations. (b) Bulk single crystal oriented for mechanical twinning, showing a high density of wide stacking faults and isolated partial dislocations. (a) and (b) have the same magnification.

Evidence for the activity of a secondary slip system in the early stages of deformation was also observed by TEM analysis of the [5422]-oriented micro-pillars. This is very likely due to the fact that the Schmid factors of both, the primary and secondary slip system were not too different. The dislocation nucleation stage was analyzed by TEM using samples fabricated from deformed micro-pillars which had experienced one or two small strain bursts in a compression test. The corresponding true strain was about 0.02. The TEM micrographs (Fig. 7) show that the small strain bursts were caused by perfect dislocation glide rather than twinning and that dislocation interactions were already prevalent. The stacking faults were found to originate from dislocation intersections, as indicated by arrows in Fig. 7a and b. The dislocation density in the deformed micro-pillars was estimated to be about $7 \times 10^{12}\ m^{-2}$. No twins were found in these micro-pillars, but in locations where dislocations had interacted on intersecting slip planes, which could have resulted in the formation of dislocation locks, wide isolated stacking faults were emitted. These stacking faults were clearly not emitted from the free surface of the micro-pillars (Fig. 7b).

3.4. ε-Martensite formation

Fig. 8 shows TEM micrographs and corresponding selected area diffraction patterns taken from the area indicated by a circle in Fig. 5c. The micro-pillar was oriented for deformation twinning, but the deformation also resulted in the formation of strain-induced ε -martensite in addition to the mechanical twins. The orientation relationship between the parent austenite and the ε-martensite was found to be the $<1\text{–}10>_\gamma//<11\text{–}20>_\varepsilon$, $(111)_\gamma//(0001)_\varepsilon$ Shoji-Nishiyama orientation relationship [26]. The dark field micrograph in Fig. 8b shows an ε-martensite platelet with a thickness of 109 nm and a number of narrower ε -martensite platelets alternating with twinned regions. The platelets had a thickness of about 20 nm. The twinned and transformed parts of the micro-pillar are indicated in the SEM micrograph of the deformed micro-pillar shown in Fig. 5e. The characteristic microstructures of twins and ε-martensite are readily visible in the high resolution lattice images shown in Fig. 8c and d. The lattice parameters of austenite, a_γ, and ε -martensite, a_ε and c_ε, were found to be approximately to 0.369 nm, 0.258 nm and 0.421 nm, respectively. The c/a ratio of the ε-martensite was 1.632.

4. Discussion

4.1. The mechanical size effect

A 'smaller is stronger' trend is often observed in small scale mechanical tests [10]. Dou and Derby [27] suggested the following scaling law for the size dependence of the shear flow stress of micro-pillars:

$$\tau/\mu = A(D/b)^m \quad (1)$$

Here τ is the resolved shear stress, μ is the shear modulus, D is the micro-pillar diameter, and b is the magnitude of the Burgers vector. The analysis of the compression test results for many pure metal fcc single crystal micro-pillars has shown to yield a value for A of 0.71 and for m of −0.6, respectively [28,29]. The Dou–Derby relation was apparently derived for pure metals without correcting the data for composition-dependent effects, such as solid solution hardening, or strain hardening.

The value of b for the TWIP steel used in the present work was 0.261 nm. The experimentally measured room temperature values of μ were 67 GPa and 77 GPa for the [5422] and [16623] orientation, respectively. The relationship between the flow stress and the micro-pillar diameter is plotted in Fig. 9a and compared to the Dou–Derby relation [27]. The values for A and m were 2.04 and −0.7, respectively, for [5422]-oriented micro-pillars and 1.37 and −0.71 for [16623]-oriented micro-pillars. Zou et al. [29] suggested an equation for the size and temperature dependence of the strength in bcc alloys. In their analysis they argued that the difference between the calculated and measured values of τ/μ was due to solid-solution hardening. It is clear that both, size-dependent and composition-dependent effects, must be taken into account. In the present study, the sample size dependent yield stress for bulk single crystal and micro-pillars was calculated by considering all contributions to the strength.

4.1.1. Bulk single crystal and polycrystalline TWIP steel

In the case of polycrystalline TWIP steel, the effect of deformation twinning as a plasticity-enhancing mechanism, solid-solution hardening contribution of the alloying elements, and the influence of the grain size on the flow stress have been studied thoroughly [30,31]. The yield stress, σ_{YS}, of polycrystalline TWIP steel has been shown to follow the Hall–Petch relationship [32]:

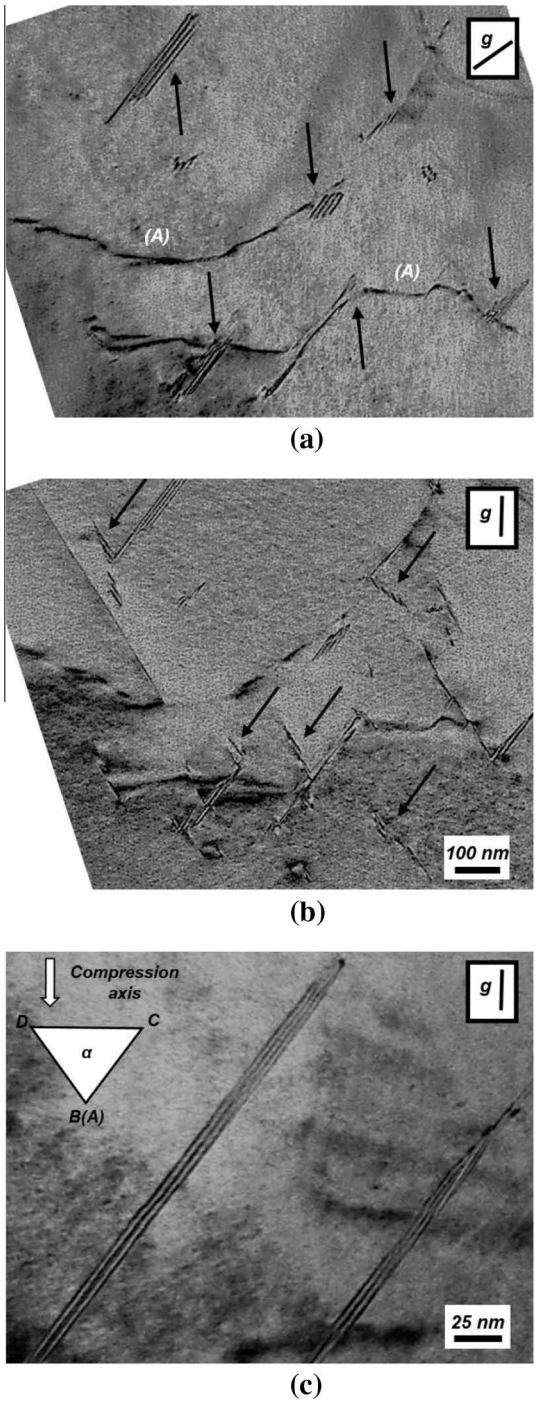

Fig. 7. TEM micrographs of a [5422]-oriented micropillar deformed up to the observation of a first strain burst. Bright-field micrographs ((a) $\boldsymbol{g} = (\bar{1}\bar{1}1)$, (b) $\boldsymbol{g} = (002)$), showing long dislocation segments (A) and stacking faults emitted from dislocation junctions (arrows). (c) Isolated wide stacking faults in the interior of the micropillar. The dislocation density of the micropillars was about 7×10^{12} m^{-2}.

$$\sigma_{YS} = \sigma_{YS}^{0} + \frac{k_{YS}^{HP}}{\sqrt{d}} \tag{2}$$

Here the parameter σ_{YS}^{0} includes the lattice friction stress, i.e. the solid solution strengthening contribution of the alloying elements, and the strain hardening contribution of the initial dislocation density, k_{YS}^{HP} is the dislocation un-pinning parameter at the yield point, d is the grain size, σ_{YS}^{0} and k_{YS}^{HP} have been reported to be equal to 132 MPa and 449 MPa μm$^{1/2}$, respectively, for polycrystalline Fe-22 wt%Mn-0.6 wt%C TWIP steel [31]. The σ_{YS}^{0} value given in the original manuscript seems to be mistyped since the yield stress level is significantly lower than the value calculated using Eq. (2) with the constants from the same reference. The value of σ_{YS}^{0} was therefore re-evaluated using the yield stress values measured for polycrystalline Fe-22 wt%Mn-0.6 wt%C TWIP steel. This corrected value for σ_{YS}^{0} was determined to be 242 MPa, rather than 132 MPa, as reported by Bouaziz et al. [31], and the corresponding critical shear stress was 79 MPa, assuming a Taylor factor of 3.06. This value is similar to the value of the yield shear stress for bulk single crystal of TWIP steel mentioned in Section 3.1.

4.1.2. Critical resolved shear stress calculation

The flow shear stress, τ_{tot}, can be expressed by the sum of the intrinsic Peierls lattice resistance to dislocation glide and additional strengthening contributions:

$$\tau_{tot} = \tau_P + \tau_{s-s} + \tau_d + \tau_s \tag{3}$$

Here τ_P denotes the Peierls stress, τ_{s-s} is the solid solution hardening due to substitutional and interstitial alloying elements, and τ_d is the strengthening from dislocation–dislocation interactions. The dislocation source size-controlled term, τ_s, is included to take the effect of the crystal size into account [13].

The following equation was used to obtain the temperature dependence of the Peierls shear stress [33]:

$$\frac{\tau_P(T)}{\mu(T)} = \frac{\tau_P(0)}{\mu(0)} \left\{ 1 - \left[\frac{kT}{g_0 \mu(T) b^3} \ln\left(\frac{\dot{\varepsilon}_0}{\dot{\varepsilon}}\right) \right]^{1/q} \right\}^{1/p} \tag{4}$$

Here, k_B is the Boltzmann constant, g_0 is a normalized activation energy with a value of 0.13 [34], $\dot{\varepsilon}$ is the strain rate, $\dot{\varepsilon}_0$ is a reference shear strain rate, which is equal to 10^8 s^{-1} [35], p and q are equal to 1/2 and 3/2, respectively, $\mu(0)$ is the shear modulus at 0 K, which was calculated by means of the following equation [36]:

$$\mu(0) = \mu(T)[1 - 7.9921 \times 10^{-7} T^2 + 3.317 \times 10^{-10} T^3]^{-1} \tag{6}$$

The Peierls stress for edge dislocations at 0 K, $\tau_P(0)$, is given by [37,38]:

$$\tau_P^{edge}(0) = \frac{\mu}{1-\nu} \exp\left[\frac{-2\pi}{1-\nu} \cdot \frac{d_{\{111\}}}{b}\right] \tag{7}$$

The Peierls stress for screw dislocations at 0 K, $\tau_P(0)$, is given by [37,38]:

$$\tau_P^{screw}(0) = \mu \exp\left[-2\pi \cdot \frac{d_{\{111\}}}{b}\right] \tag{8}$$

The Poisson's ratio ν is equal to 0.312 [34]. The ratio of the effective {1 1 1} interplanar spacing and the magnitude of the Burgers vector, $\frac{d_{\{111\}}}{b}$, is equal to 1.1547, using $d_{\{111\}} = \sqrt{6}/3a_\gamma$ [35,36]. The calculated τ_P at 297 K is 0.14 MPa and 2.64 MPa for edge and screw dislocations, respectively, τ_P was set equal to the mean value of both values, 1.39 MPa.

The solid solution hardening effect of C in Fe-22%Mn-0.6%C TWIP steel on the yield shear stress was obtained experimentally by varying the C content of a Fe-x%C-15%Mn-2%Al-1%Si TWIP steel in the range of 0.78–0.92 wt%. The results, shown in Fig. 10, indicate a solid solution hardening effect on the shear stress of 91.3 MPa per wt%C. The solid solution hardening effect of Mn was taken as −0.59 MPa per wt%Mn [34]. As a result, the τ_{s-s} was equal to 44.0 MPa for the Fe-22 wt%Mn-0.6 wt%C TWIP steel. Note that these solid solution hardening effects must be multiplied by 3.06 to obtain the solid solution strengthening effect in tensile deformation.

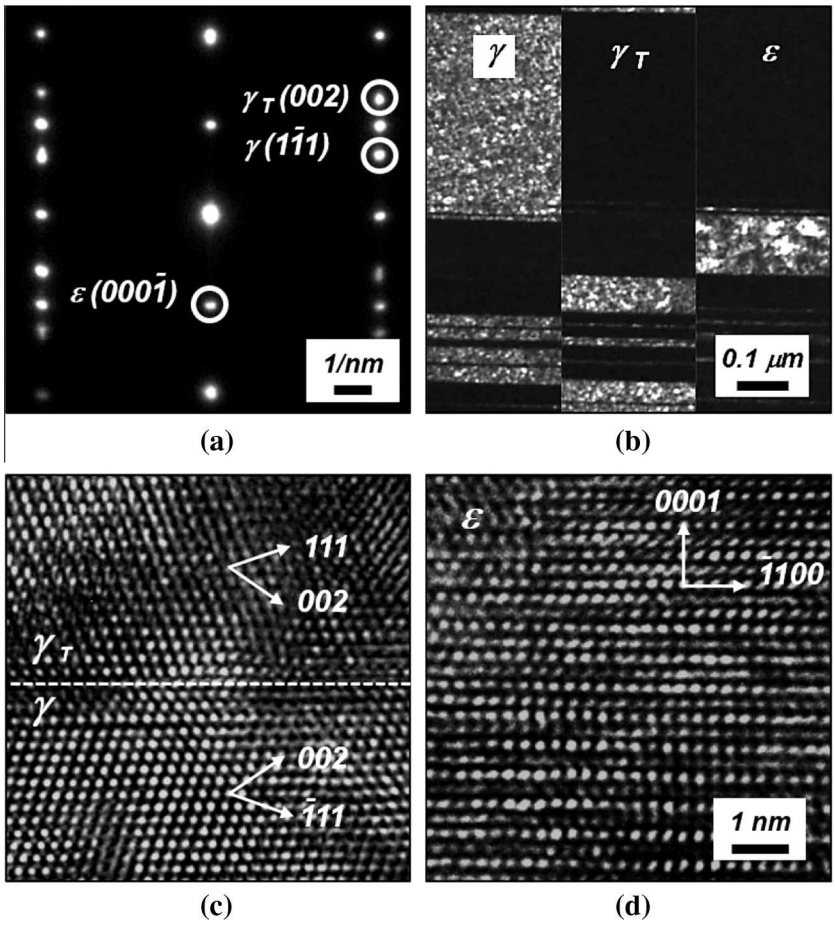

Fig. 8. TEM micrographs of a deformed micropillar oriented for deformation twinning. (a) Selected area diffraction pattern indicating the presence of twins and ε-martensite. (b) Dark field micrographs showing twins and ε-martensite in the parent austenite matrix. High resolution micrographs of (c) twinned region and (d) ε-martensite plate.

The dislocation–dislocation interactions lead to a strain hardening contribution τ_d described quantitatively by the Hirsch–Bailey equation:

$$\tau_d = \alpha\mu b\sqrt{\rho_d} \tag{9}$$

Here α is a constant and ρ_d is the total dislocation density. The value of α is 0.35. The measured dislocation density in the micro-pillar was about 7×10^{12} m^{-2}. The value of τ_d, obtained by means of Eq. (9), was therefore 15.7 MPa.

Several models have been proposed to explain the crystal size dependence of the critical shear stress [13,39–41]. Parthasarathy et al. [13] suggested that double-ended dislocation sources in micro-pillars could easily become single-ended dislocation sources by interaction with a free surface. This process should result in strengthening when testing micron-size samples such as micro-pillars. The strength of single-ended and double-ended sources in small crystals calculated by discrete dislocation dynamics simulations, support the following type of dislocation source size dependence [14]:

$$\tau_s = K\frac{\mu b}{L}\ln\left(\frac{L}{b}\right) \tag{10}$$

Here K is a source-hardening constant, which is 0.12 for a single-ended dislocation source. The calculated effect of image forces on the critical resolved shear stress for dislocation sources larger than 250b has been shown to be negligible [14].

The following dislocation segment length dependence of the line tension stress was included in the model for the shear stress acting on a dislocation segment of length L [42]:

$$\tau_s = \frac{\mu b}{L}\frac{1}{2\pi(1-\nu)}\left[\left(1-\frac{3}{2}\nu\right)\ln\left(\frac{L}{b}\right)+\frac{\nu-2}{2}\right] \tag{11}$$

Eqs. (4) to Eq. (10) were combined to obtain the following equation for τ_{tot}:

$$\frac{\tau_{tot}}{\mu} = \frac{\tau_P(0)}{\mu(0)}\left\{1-\left[\frac{kT}{g_0\mu(T)b^3}\ln\left(\frac{\dot{\varepsilon}_0}{\dot{\varepsilon}}\right)\right]^{1/q}\right\}^{1/p} + \frac{\tau_{s-s}}{\mu} + \alpha b\sqrt{\rho_d} + \frac{b}{L}\frac{1}{2\pi(1-\nu)}\left[\left(1-\frac{3}{2}\nu\right)\ln\left(\frac{L}{b}\right)+\frac{\nu-2}{2}\right] \tag{12}$$

Norfleet et al. [40] reported that the model containing measured dislocation density and size-dependent source strengthening was not sufficient to explain the observed yield stress of micro-pillars. Zou et al. [29] used a higher value of 0.5 for K, assuming that the dislocation source length was limited by the diameter of the micro-pillar. The correct micro-pillar diameter dependence of the effective source length, L_{eff}, can, however, be obtained by combining Eqs. (1) and (12):

$$\frac{\mu b}{L_{eff}}\frac{1}{2\pi(1-\nu)}\left[\left(1-\frac{3}{2}\nu\right)\ln\left(\frac{L_{eff}}{b}\right)+\frac{\nu-2}{2}\right] = A\mu(D/b)^m - (\tau_P + \tau_{s-s} + \tau_d) \tag{13}$$

Fig. 11 shows the size dependence of L_{eff}. The value of L_{eff} increases asymptotically for a micro-pillar with a critical diameter. With decreasing pillar size, the dislocation source size must necessarily become smaller and the ratio of the effective source length and the micro-pillar diameter, L_{eff}/D, decreases. Eq. (13) also allows for the determination of the critical pillar size for bulk behavior. The critical diameter is about 7.6 μm where the effective source

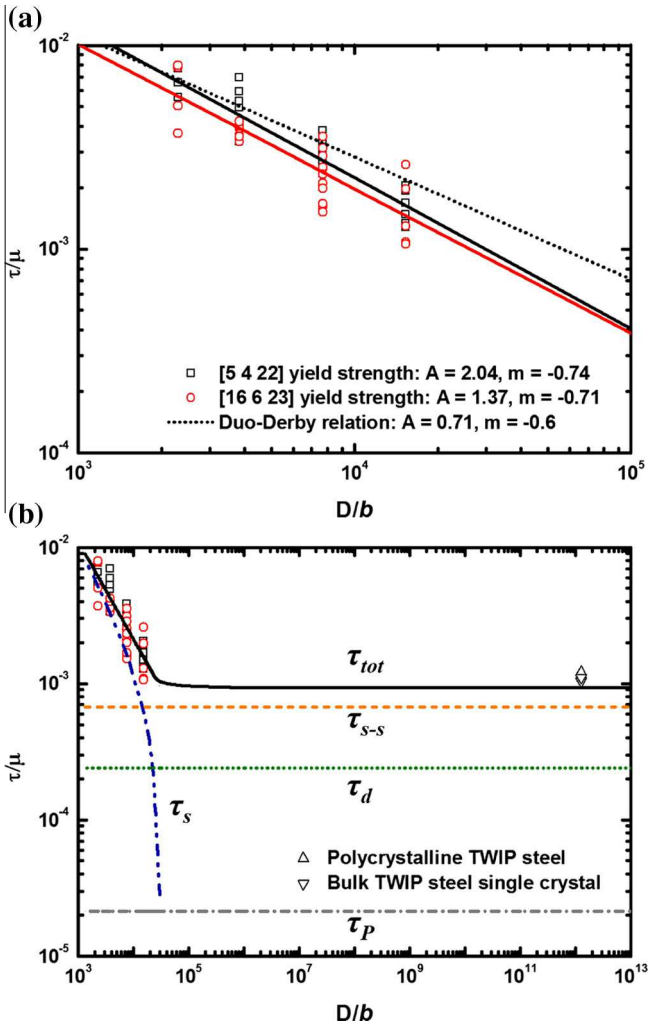

Fig. 9. (a) Relationship between normalized yield shear stress τ/μ and micropillar diameter. The original Dou–Derby equation [25] for fcc crystals is also indicated, as well as the equations which apply to the TWIP steel micropillars. (b) Calculated total shear strength, τ_{tot}, considering the contributions of the Peierls stress, τ_P, solid solution hardening, $\tau_{s\text{-}s}$, strain hardening, τ_d, and the source-controlled contribution, τ_s. The critical transition size from micropillar to bulk behavior occurs at about 7.6 μm.

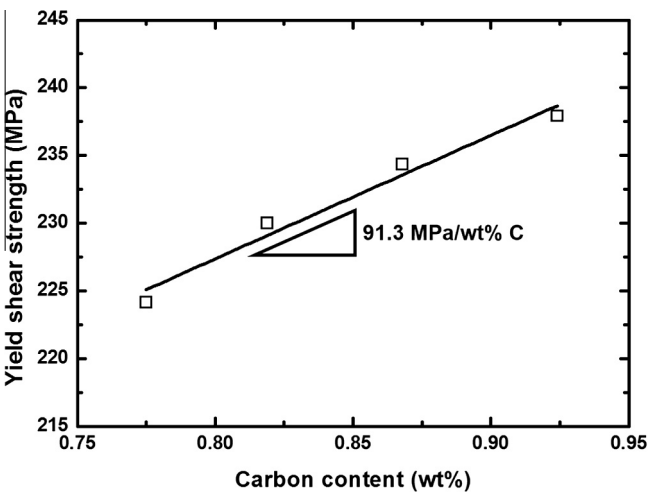

Fig. 10. Solid solution hardening effect of C of the yield shear stress of Fe-15Mn-2Al-1Si-xC TWIP steel.

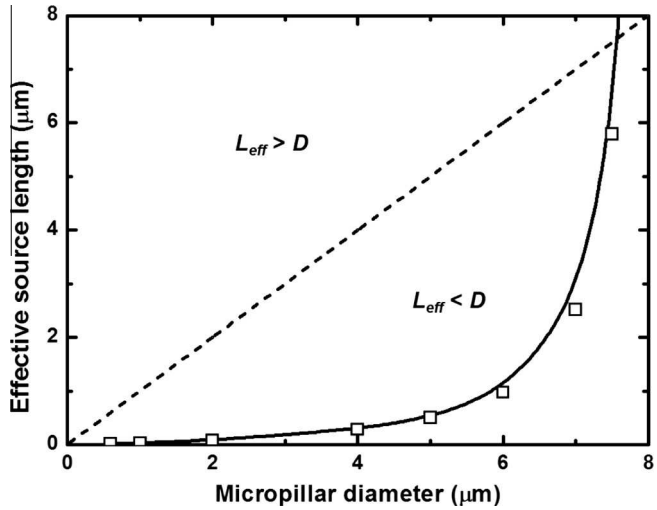

Fig. 11. Size dependence of the effective source size, L_{eff}, in TWIP steel micropillars. The critical micropillar diameter is 7.6 μm, corresponding to the condition that the effective source length is equal to the micropillar diameter.

length is equal to the micro-pillar diameter. This value is a calculated value, based solely on model calculations, as the maximum pillar diameter used in the present study was 4 μm.

Fig. 9b shows the experimentally observed and calculated shear stress for yielding as a function of L_{eff}. The contribution of each strengthening mechanisms is indicated in the figure. It is clear that Eq. (12) captures the observed size dependence of the shear stress of Fe-22 wt%Mn-0.6 wt%C TWIP steel. The effect of the size-controlled stress is significantly reduced when the micro-pillar size approaches the critical diameter of 7.6 μm. The calculated sample-size independent critical resolved shear stress, τ_{CRSS}, for yielding at room temperature is, therefore, given by the sum $\tau_P + \tau_{s-s} + \tau_d$, i.e. 61.1 MPa for Fe-22 wt%Mn-0.6 wt%C. This value is slightly smaller than the experimentally measured τ_{CRSS} of 75.7 MPa for polycrystalline TWIP steel. The difference is very likely due to the underestimation of the dislocation density in the polycrystalline TWIP steel. Eq. (9) was used to determine the actual dislocation density of the polycrystalline TWIP steel:

$$\rho_d = \left(\frac{\tau_{CRSS} - \tau_P - \tau_{s-s}}{\alpha \mu b}\right)^2 \tag{14}$$

The initial dislocation density of polycrystalline TWIP steel is 2.6×10^{13} m^{-2}, rather than 7×10^{12} m^{-2}. This result is similar to the value reported earlier (6.4×10^{13} m^{-2}) for polycrystalline TWIP steel [43].

Subtracting τ_{s-s} from the experimentally measured τ_{CRSS}, and taking into account the solid solution strengthening contributions of Mn, Al and Si reported in the literature [34,44], the following equation was obtained for the composition dependence of the size independent τ_{CRSS} of Fe–Mn–C–Al–Si austenitic TWIP steel:

$$\tau_{CRSS} = 31.7\ \text{MPa} + 91.3\ \text{MPa/wt\%C} - 0.49\ \text{MPa/wt\%Mn} + 16.2\ \text{MPa/wt\%Si} + 6.7\ \text{MPa/wt\%Al} \tag{15}$$

4.2. Partial dislocation-mediated plasticity of TWIP steel

In polycrystalline TWIP steels, the elasto-plastic transition has been reported to be associated with perfect dislocation glide and the formation of isolated stacking faults which appear to be emitted by grain boundaries [45]. Grain boundaries have also been reported to act as sources of deformation twins [46]. Mahajan

and Chin [47] suggested that twin nuclei, formed by three stacking faults on adjacent {1 1 1} planes, could grow into twins by a collective bow-out mechanism between pinning points. Deformation twinning may also occur after dislocation–dislocation interactions which result in configurations, such as suitably oriented sessile jogs of screw-type dislocations, which can act as twin sources by a pole mechanism [48]. Experimental observations by TEM suggest that twin nucleation, due to the operation of the pole mechanism, occurs in the early stages of deformation [49]. In the course of the present work, TEM analysis of pillars compressed up to the observation of the first strain burst was carried out, and no deformation twins or strain-induced ε-martensite plates were observed.

4.2.1. Elasto-plastic transition

During the elasto-plastic transition, dislocation sources become active. The maximum dislocation source length in a micro-pillar is limited by the pillar size. Single-ended dislocation sources have been reported to be the dominant dislocation sources in the micro-pillars [13] and in thin TEM foils which were strained in the microscope [50]. The size of a single-ended dislocation was much smaller than the size of a double-pinned Frank-Read source, which was in the range of 160–500 nm in in-situ strained TEM samples [50]. Dislocations nucleated from a single-ended source can easily escape out of a micro-pillar during deformation without dislocation pile-up formation or interactions leading to sessile dislocation junctions [50]. Greer et al. [12] suggested that the minimum travel distance required for dislocation multiplication was of the order of 1 μm in Ag. They reported that micro-pillars with a diameter smaller than 0.7 μm had a higher flow stress than expected from a general power law. They argued that this was due to dislocation starvation occurring before dislocation multiplication. Here, evidence of dislocation–dislocation interactions in the initial stage of deformation was obtained from TEM analysis of micro-pillars which had been strained until the first and second strain burst was observed. These strain bursts were due to dislocation sources, which rapidly produced avalanches of mobile dislocations.

The energy for the activation of a perfect dislocation Frank-Read source and a partial dislocation twin source can be computed as the energy required to nucleate a perfect dislocation loop, $E_{perfect}$, and a partial dislocation loop, E_{twin}, respectively [42]:

$$E_{perfect} = -\pi R^2 \tau b + \frac{1}{2}\mu b^2 R \frac{2-\nu}{2(1-\nu)}\left(\ln\frac{4R}{r} - 2\right) \tag{16}$$

and

$$E_{twin} = -\pi R^2 \tau b_p + \frac{1}{2}\mu b^2 R \frac{2-\nu}{2(1-\nu)}\left(\ln\frac{4R}{r} - 2\right) + \pi R^2 \gamma_{SF} \tag{17}$$

Here ρ is the core radius of the dislocation, which is assumed to be equal to the Burgers vector and R is a dislocation loop radius. Fig. 12 shows the dislocation loop size dependence of the activation energy of dislocation loops for the measured average yield shear stresses of micro-pillars with different diameters. The curves show that the energy barrier for source activation reaches a maximum at the critical stress. The maximum energy barrier occurs at a critical dislocation loop size corresponding to the condition $\partial E/\partial R|_{R=R_c} = 0$. Fig. 13a and b show the applied shear stress dependence of the critical dislocation loop size and critical nucleation energy. The figure also indicates the average critical resolved shear stress measured for the micro-pillars in this work. The difference in critical loop size at an applied shear stress smaller than 200 MPa

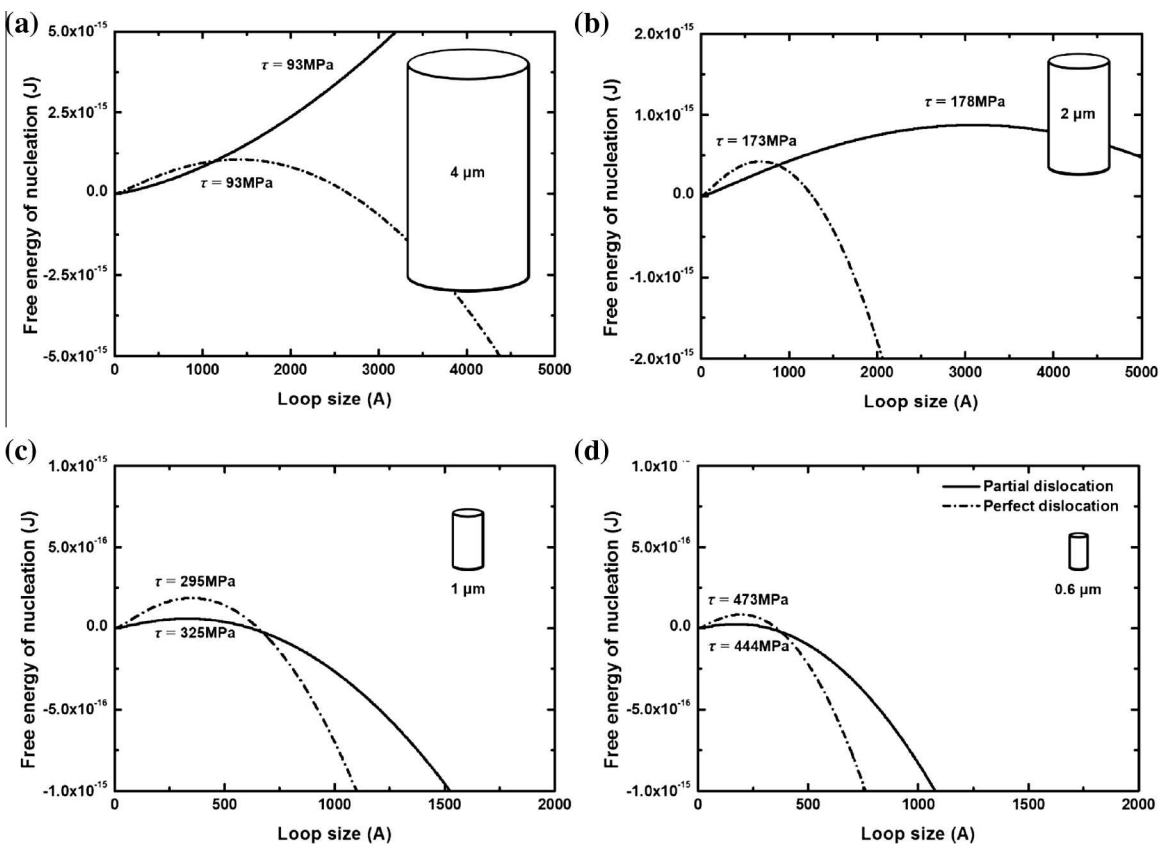

Fig. 12. Dislocation loop size dependence of the nucleation energy of a partial dislocation twin source and of a perfect dislocation Frank-Read source for micropillars with a diameter of (a) 4 μm, (b) 2 μm, (c) 1 μm, and (d) 0.6 μm. The experimentally measured critical shear stress is indicated for each of the calculated curves. The cylinders give an idea of the relative dimensions of the micropillars.

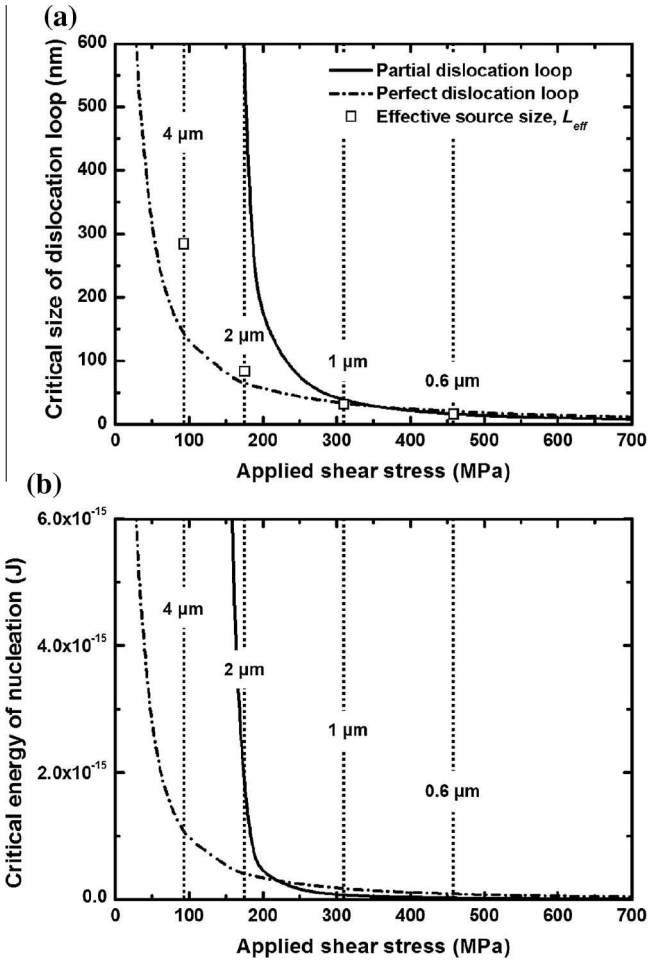

Fig. 13. Applied shear stress dependence of (a) the critical size with the effective source size, L_{eff}, and (b) the critical energy of nucleation of a partial dislocation half loop and a perfect dislocation half loop. The partial dislocation loop is unstable at an applied shear stress lower than 150 MPa. The vertical lines indicate the applied shear stress required to reach the point of dislocation half loop instability for the micropillar diameters used in the present work.

increased exponentially, resulting in the divergence of the critical loop size at an applied shear stress of about 150 MPa. It is notable that L_{eff} obtained from Eq. (13) was in accordance with the calculated critical size for a perfect dislocation loop. A similar trend was shown for the critical energy of nucleation. As the applied shear stress increased due to the size effect, the critical size and energy of nucleation of partial and perfect dislocation loops became comparable. The critical shear stress for yielding of [011]-oriented and [001]-oriented bulk single crystal was 76 MPa and 72 MPa, respectively. It is thus unlikely that a partial dislocation source was activated at such low stresses, since a partial dislocation source cannot achieve instability and expand at such a low stress level. In addition, the critical resolved shear stresses for yielding of [5422]- and [16623]-oriented micro-pillars were similar as shown in Fig. 4. The calculation and the experimental observation imply that the elasto-plastic transition in the micro-pillars and the bulk single crystals oriented for twinning is achieved by a dislocation mechanism that does not involve twinning.

4.2.2. Mechanisms for twinning and ε-martensite formation

The deformation mechanisms of polycrystalline TWIP steel with various SFE were experimentally determined by Allain et al. and γ → ε-martensite transformation was only observed in Fe-22 wt%Mn-0.6 wt%C TWIP steel deformed at 77 K [51]. In the present study, the strain-induced γ → ε transformation was, however, observed during micro-pillar compression at room temperature. This observation can be understood by consideration of the applied shear stress dependence of the effective SFE, γ_{eff}. γ_{eff} is defined as follows [21,22]:

$$\gamma_{eff} = \gamma_0 + \frac{m_t - m_l}{2}\tau_A b \tag{18}$$

Here γ_0 is the equilibrium SFE in the absence of an applied stress, m_t and m_l are the Schmid factor of the trailing and leading partial dislocations, respectively, and τ_A is the applied shear stress. The applied shear stress dependence of γ_{eff} and the stress at which large strain bursts were experimentally observed are indicated in Fig. 14. γ_{eff} could clearly be reduced to a value much lower than the value of the SFE required for the γ → ε transformation in high stress conditions. This implies that the γ → ε transformation became energetically favorable in micro-pillars oriented for partial dislocation glide in compression tests. As the applied stress increased, the stacking fault width increased substantially, allowing the strain-induced γ → ε phase transformation to occur [52].

Fig. 15 shows a schematic of the deformed micro-pillars. The mechanisms which explain the observed deformation twinning and dislocation glide in the micro-pillars are also indicated. The small cube in the figure corresponds to the unit cell orientation in the [16 6 23]-oriented and [5 4 22]-oriented micro-pillar. The primary slip system is enlarged to make the dislocation configuration clear. In order to generate perfect dislocations, it is proposed that screw segments of the primary slip system could easily cross-slip twice due to the reduced stacking fault width, which also resulted in the observed wave-like slip traces shown in Fig. 5f. Once double cross-slip had occurred, Frank-Read type dislocation sources were generated as shown in Fig. 15a [42] and easily became single-ended dislocation sources due to the size of the micro-pillar [13]. The successive generation of perfect dislocation loops from a single dislocation source also explains why the shear deformation of micro-pillars oriented for perfect dislocation glide was highly localized (Fig. 5d).

In the case of micro-pillars oriented for twinning, it is postulated that a screw type pole dislocation allowed for the formation

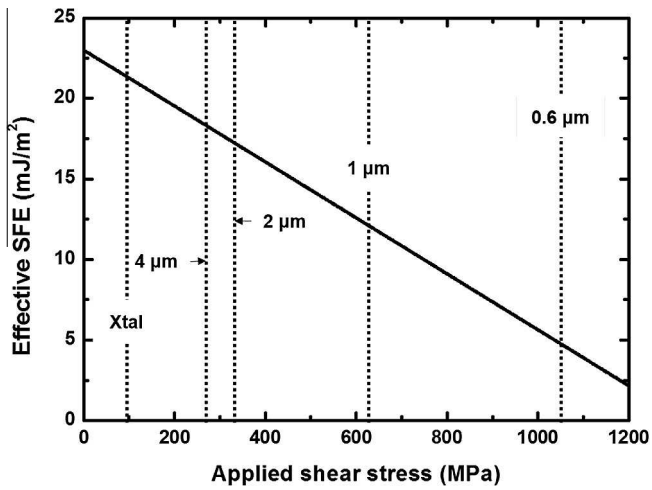

Fig. 14. Applied shear stress dependence of the effective stacking fault energy for a [5422]-oriented pillar deformed in compression. The vertical lines indicate the mean shear stress of large strain bursts for the micropillars with the indicated diameter. The shear yield stress of the bulk single crystal (Xtal) is also indicated. The effective stacking fault energy decreases with decreasing micropillar diameter, resulting in strain-induced γ → ε transformation in condition where the equilibrium SFE is about 23 mJ/m².

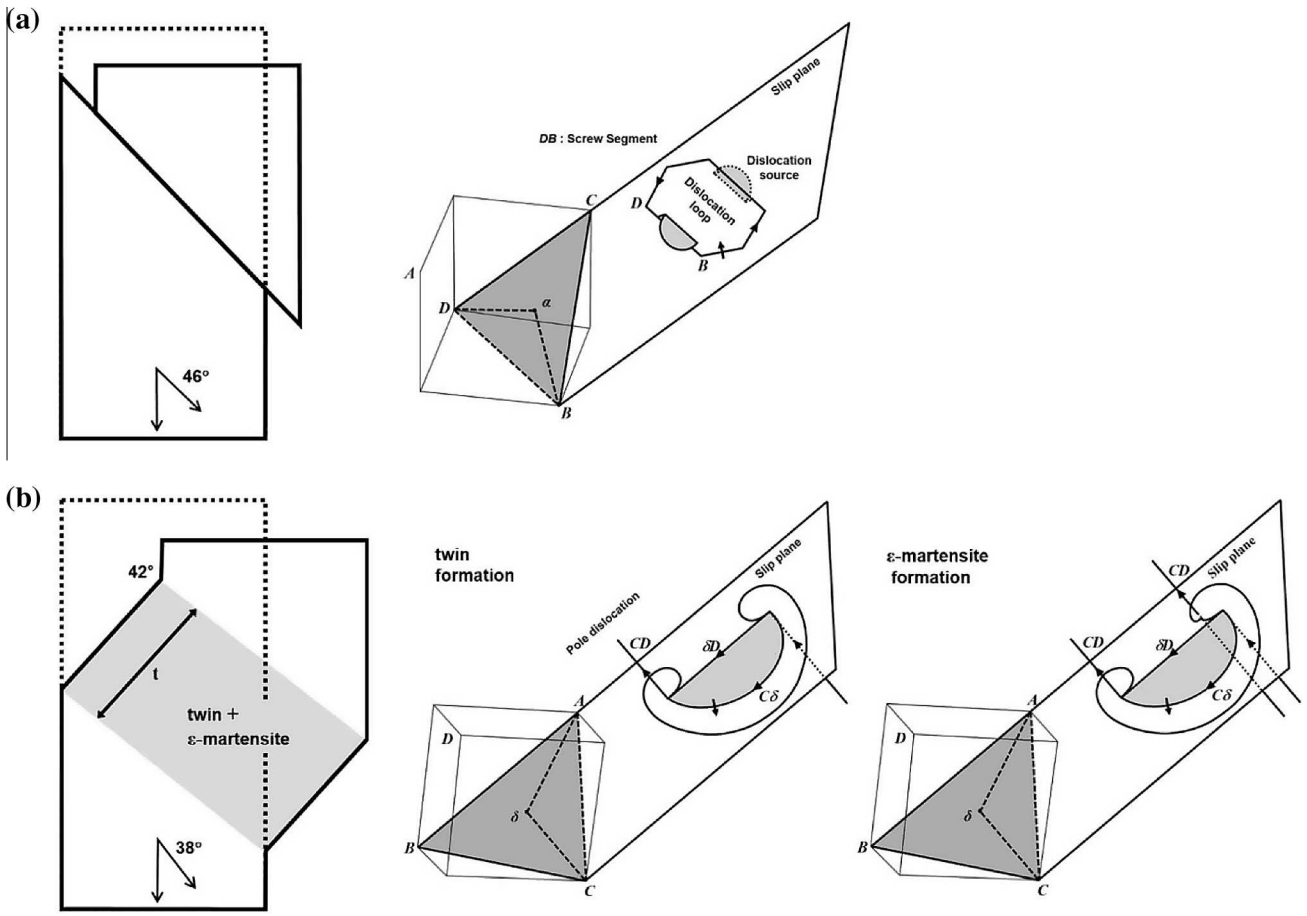

Fig. 15. Schematic of the deformation mechanisms in micropillars oriented for (a) dislocation glide and (b) deformation twinning. In (a) the localized deformation is due to the activation of a Frank-Read dislocation source formed by the double cross-slip mechanism. Double cross-slip is preferential due to the high effective SFE. In (b) the formation of a mechanical twin and/or an ε-martensite platelet is by the screw dislocation pole mechanism. The formation of the ε-martensite plate is due to a double pole mechanism.

of a twin by spiraling of the ***δC*** twinning partial dislocation around the ***CD*** screw type pole dislocation segments on either side of the jog, as shown in Fig. 15b [42,51]. If two screw dislocations were acting as pole dislocation instead of one, the partial dislocation ***δC*** would glide on every second slip plane (Fig. 15b) and this could result in the formation of ε-martensite. The mechanism is a straightforward extension of the twinning formation mechanism proposed by Niewczas and Saada [53]. No geometrical difficulty exists to grow ε-martensite by a similar pole mechanism except for the stress barrier associated with the Frank dislocation. Double-pole dislocation configurations have been observed experimentally by TEM [53]. The ε-martensite formation mechanism is shown in detail in Fig. 16. The indicated dislocations correspond to those for the [5422]-oriented micro-pillar. The figure shows two segments of a primary pole dislocation with a Burgers vector ***CD*** connected by two nodes N_1 and N_2. An additional pole dislocation with the same Burgers vector, adjacent to the primary pole dislocations, allow for the partial dislocation ***δC*** to glide on every second slip plane, resulting in the formation of an ε-martensite platelet.

In this model it was assumed that the nature of the stacking fault was intrinsic. The available reports on the analysis of the nature of stacking faults in high Mn austenitic steels analysis disagree. Whereas Idrissi et al. [49] report that the stacking faults are extrinsic, based on their analysis of stacking fault fringe contrast, Pierce et al. [54], using conventional diffraction contrast, more recently concluded that the stacking faults were intrinsic. Furthermore, we observed only intrinsic stacking faults in the present study and, therefore, did not further consider extrinsic stacking faults as nuclei for ε-martensite formation.

Using the high resolution SEM (Fig. 5) and TEM (Fig. 7) micrographs, the strain contributed by mechanical twinning and strain-induced ε-martensite formation was determined. In Fig. 15b, the total thickness, **t**, of the twinned region and ε-martensite plate was 1139 nm in the micro-pillar at a total true plastic strain of 0.18. The angle between the matrix and the transformed plane was 42°. Partial dislocations glide on every slip plane in the case of a twin and on every second slip plane in the case of a ε-martensite platelet. The corresponding amount of deformation was 0.07 true strain. The remaining plastic strain of about 0.10 must have been contributed by dislocation glide and dislocation avalanches, which were visible as sharp slip traces in the deformed micro-pillars. In the case of the [5422]-oriented micro-pillars, the secondary slip system has probably been activated at a low stress level, since the Schmid factor for the secondary slip plane was close to the Schmid factor of the primary slip system. This resulted in the dislocation intersections shown in the TEM micrograph of Fig. 7a and b. It is postulated that in the present case these structural defects acted as source for the dislocations required for the mechanisms shown in Fig. 15. Another possibility is that the inelastic Ga^+ ion–solid interactions within the sample, occurring during the FIB sample preparation may have resulted in the formation of dislocation loops. Such inelastic Ga^+ ion–solid interactions are known to cause lattice damage and introduce point defects

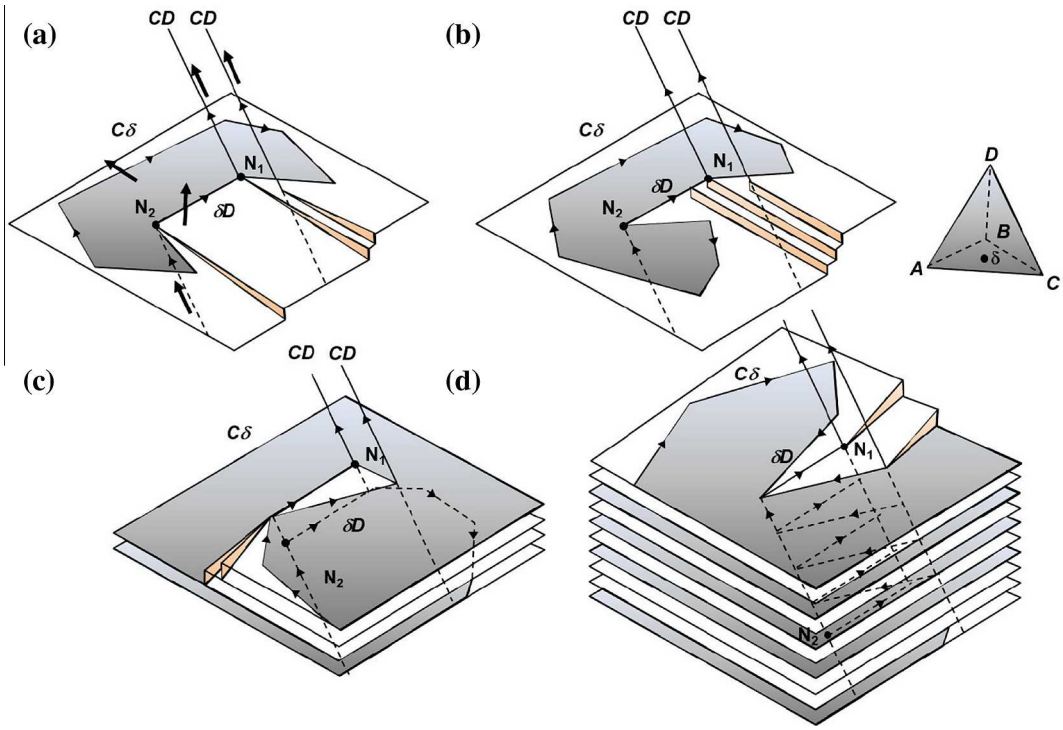

Fig. 16. Schematic of ε-martensite formation by a double screw dislocation pole mechanism. (a) Nucleation of the partial dislocation ***Cδ*** on a large jog segment on the screw dislocation ***CD***. (b) Break-away of the partial dislocation ***Cδ*** after reaching its critical loop diameter. (c) Spiraling movement of the partial dislocation ***Cδ*** around the two pole dislocations. (d) The presence of the two screw dislocations with Burgers vector ***CD*** acting as poles, causes the partial ***Cδ*** to spiral around, and being displaced by two {1 1 1} planes for each rotation. This leads to the generation of the stacking sequence of hcp ε-martensite. The ε-martensite plate thickens with each partial dislocation rotation.

and it has been experimentally observed that point defect clusters and planar defects can be produced by ion-beam processing [55,56].

5. Conclusions

The plastic deformation of single crystal micro-pillars of Fe-22%Mn-0.6%C TWIP steel oriented for perfect dislocation glide and deformation twinning was analyzed by means of compression tests conducted in a nano-indentation setup. The main conclusions of the present work are as follows:

1. The critical resolved shear stress of micro-pillars oriented for deformation twinning and micro-pillars oriented for dislocation glide were similar. The result suggests that the elasto-plastic transition of the micro-pillars is due to dislocation glide, independent of the fact that the orientation may favor twinning.
2. The following equation was obtained for the composition dependence of the room temperature τ_{CRSS} of Fe–Mn–C–Al–Si austenitic TWIP steel:

$$\tau_{CRSS} = 31.7\ \text{MPa} + 91.3\ \text{MPa/wt\%C} - 0.49\ \text{MPa/wt\%Mn} + 16.2\ \text{MPa/wt\%Si} + 6.7\ \text{MPa/wt\%Al}$$

3. Highly localized shear deformation occurred in micro-pillars oriented for dislocation glide.
4. Strain-induced $\gamma \rightarrow \varepsilon$ transformation is not observed in bulk Fe-22%Mn-0.6%C TWIP steel. In micro-pillars oriented for deformation twinning both twinned regions and regions which had transformed to ε-martensite were observed.
5. The critical micro-pillar diameter for size-independent plasticity was determined to be approximately 7.6 μm.

Acknowledgements

Mr. Won Seok Choi and Dr. B.C. De Cooman gratefully acknowledge the support of the POSCO Technical Research Laboratories, Gwangyang, South Korea. Dr. D. Raabe and Dr. S. Sandlöbes gratefully acknowledge the support of the Deutsche Forschungsgemeinschaft (DFG), Germany, through the collaborative research centre SFB 761 'Steel ab initio'.

References

[1] M. Niewczas, Chapter 75, Dislocations in Solids, in: F.R.N. Nabarro, J.P. Hirth (Eds.), Elsevier BV, 2007, pp. 264–364.
[2] S.R. Kalidindi, A.A. Salem, R.D. Doherty, Adv. Eng. Mater. 5 (2003) 229–232.
[3] O. Bouaziz, N. Guelton, Mater. Sci. Eng. A 319–321 (2001) 246–249.
[4] S. Mahajan, Philos. Mag. 23 (1971) 781–794.
[5] C.W. Price, J.P. Hirth, Mater. Sci. Eng. 9 (1972) 15–18.
[6] J.C.M. Li, Trans. AIME 227 (1963) 239–247.
[7] J.F. Nicholas, An Atlas of Models of Crystal Surfaces, Gordon and Breach, 1965.
[8] C.R. Weinberger, W. Cai, Proc. Natl. Acad. Sci. 105 (2008) 14304–14307.
[9] T. Zhu, J. Li, A. Samanta, K. Gall, Phys. Rev. Lett. 100 (2008) 025502.
[10] J.R. Greer, J.T.M. Hosson, Prog. Mater. Sci. 56 (2011) 654–724.
[11] M.D. Uchic, P.A. Shade, D.M. Dimiduk, Annu. Rev. Mater. Res. 39 (2009) 361–386.
[12] J.R. Greer, W.C. Oliver, W.D. Nix, Acta Mater. 53 (2005) 1821–1830.
[13] T.A. Parthasarathy, S.I. Rao, D.M. Dimiduk, M.D. Uchic, D.R. Trinkle, Scripta Mater. 56 (2007) 313–316.
[14] S.I. Rao, D.M. Dimiduk, M. Tang, T.A. Parthasarathy, M.D. Uchic, C. Woodward, Philos. Mag. 87 (2007) 4777–4794.
[15] Q. Yu, Z.-W. Shan, J. Li, X. Huang, L. Xiao, J. Sun, E. Ma, Nat. Lett. 463 (2010) 335–338.
[16] J.H. Seo, H.S. Park, Y. Yoo, T.Y. Seong, J. Li, J.P. Ahn, B. Kim, I.S. Choi, Nano Lett. 13 (2013) 5112–5116.
[17] S.Z. Wu, H.W. Yen, M.X. Huang, A.H.W. Ngan, Scripta Mater. 67 (2012) 641–644.
[18] S. Reeh, D. Music, T. Gebhardt, M. Kasprzak, T. Jäpel, S. Zaefferer, D. Raabe, S. Richter, A. Schwedt, J. Mayer, B. Wietbrock, G. Hirt, J.M. Schneider, Acta Mater. 60 (2012) 6025–6032.

[19] I. Gutierrez-Urrutia, D. Raabe, Acta Mater. 59 (2011) 6449–6462.
[20] A. Dumay, J.P. Chateau, S. Allain, S. Migot, O. Bouaziz, Mater. Sci. Eng. A 483–484 (2008) 184–187.
[21] S.M. Copley, B.H. Kear, Acta Metall. 16 (1968) 227–231.
[22] I. Karaman, H. Sehitoglu, K. Gall, Y.I. Chumlyakov, H.J. Maier, Acta Mater. 48 (2000) 1345–1359.
[23] D.M. Dimiduk, C. Woodward, R. LeSar, M.D. Uchic, Science 312 (2006) 1188–1190.
[24] A. Rinaldi, P. Peralta, C. Friesen, K. Sieradzki, Acta Mater. 56 (2008) 511–517.
[25] F. Mompiou, M. Legros, A. Sedlmayr, D.S. Gianola, D. Caillard, O. Kraft, Acta Mater. 60 (2012) 977–983.
[26] J.B. Seol, J.E. Jung, Y.W. Jang, C.G. Park, Acta Mater. 64 (2013) 558–578.
[27] R. Dou, B. Derby, Scripta Mater. 61 (2009) 524–527.
[28] M.J. Burek, J.R. Greer, Nano Lett. 10 (2009) 69–76.
[29] Y. Zou, S. Maiti, W. Steurer, R. Spolenak, Acta Mater. 65 (2014) 85–97.
[30] B.C. Cooman, O. Kwon, K.-G. Chin, Mater. Sci. Technol. 28 (2012) 513–527.
[31] O. Bouaziz, S. Allain, C.P. Scott, P. Cugy, D. Barbier, Curr. Opin. Solid State Mater. Sci. 15 (2011) 141–168.
[32] B.C. Cooman, J.G. Speer, Fundamentals of Steel Product Physical Metallurgy, third ed., AIST, Warrendale, PA, 2012.
[33] P.S. Follansbee, Fundamentals of Strength, John Wiley & Sons Inc., 2014.
[34] I. Jung, B.C. Cooman, Acta Mater. 61 (2013) 6724–6735.
[35] N. Tsuchida, Y. Tomota, H. Moriya, O. Umezawa, K. Nagai, Acta Mater. 29 (2001) 3029–3038.
[36] G. Ghosh, G.B. Olson, Acta Mater. 50 (2002) 2655–2675.
[37] J.N. Wang, Mater. Sci. Eng. A 206 (1996) 259–269.
[38] J.N. Wang, Acta Mater. 4 (1996) 1541–1546.
[39] K.S. Ng, A.H.W. Ngan, Scripta Mater. 59 (2008) 796–799.
[40] D.M. Norfleet, D.M. Dimiduk, S.J. Polasik, M.D. Uchic, M.J. Mills, Acta Mater. 56 (2008) 2988–3001.
[41] S.W. Lee, W.D. Nix, Philos. Mag. 92 (2012) 1238–1260.
[42] J.P. Hirth, J. Lothe, Theory of Dislocations, second ed., John Wiley & Sons, Inc., 1992.
[43] J. Kim, Y. Estrin, H. Beladi, I. Timokhina, K.G. Chin, S.K. Kim, B.C. De Cooman, Metall. Mater. Trans. A 66 (2012) 479–490.
[44] K. Jeong, J.E. Jin, Y.S. Jung, S. Kang, Y.K. Lee, Acta Mater. 61 (2013) 3399–3410.
[45] D.R. Steinmetz, T. Jäpel, B. Wietbrock, P. Eisenlohr, I. Gutierrez-Urrutia, A. Saeed-Akbari, T. Hickel, F. Roters, D. Raabe, Acta Mater. 61 (2013) 494–510.
[46] Z. Jin, T.R. Bieler, Philos. Mag. A 71 (1995) 925–947.
[47] S. Mahajan, G.Y. Chin, Acta. Metall. 21 (1973) 1353–1363.
[48] J.A. Venables, Philos. Mag. 6 (1960) 379–396.
[49] H. Idrissi, K. Renard, L. Ryelandt, D. Schryvers, P.J. Jacques, Acta. Mater. 58 (2010) 2464–2476.
[50] S.H. Oh, M. Legros, D. Kiener, G. Dehm, Nat. Mater. 8 (2009) 95–100.
[51] S. Allain, J.-P. Chateau, O. Bouaziz, S. Migot, N. Guelton, Mater. Sci. Eng. A 387–389 (2004) 158–162.
[52] T.S. Byun, Acta Mater. 51 (2003) 3063–3071.
[53] M. Niewczas, G. Saada, Philos. Mag. A 82 (2002) 167–191.
[54] D.T. Pierce, J.A. Jimenez, J. Bentley, D. Raabe, C. Oskay, J.E. Wittig, Acta Mater. 68 (2014) 238–253.
[55] C.A. Volkert, A.M. Minor, MRS Bull. 32 (2007) 389–395.
[56] S.O. Kucheyev, J.S. Williams, C. Jagadish, J. Zou, Phys. Rev. B 67 (2003) 094115.